Biaxial strain modulated valence-band engineering in III-V digital alloys

Sheikh Z. Ahmed,[1,*] Yaohua Tan,[2] Jiyuan Zheng,[3] Joe C. Campbell,[1] and Avik W. Ghosh[1,4]

[1]*Department of Electrical and Computer Engineering, University of Virginia, Charlottesville, Virginia 22904, USA*

[2]*Synopsys Inc., Mountain View, California 94043, USA*

[3]*Beijing National Research Center for Information Science and Technology, Tsinghua University, 100084 Beijing, China*

[4]*Department of Physics, University of Virginia, Charlottesville, Virginia 22904, USA*

(Received 7 November 2021; revised 10 May 2022; accepted 7 June 2022; published 6 July 2022)

A series of III-V digital alloy avalanche photodiodes have been recently seen to exhibit very low excess noise. These alloys have low hole ionization coefficients due to enhanced effective mass, a large separation between light-hole and split-off bands in the valence band, and in one case (InAlAs), potentially the creation of a small minigap in computed band structures. Whereas such minigaps would indeed provide a reliable way to suppress hole transport and reduce excess noise, their physical origin is explored here. In this paper, we provide an explanation for the formation of the minigaps as arising from oscillations in certain orbital overlaps. We demonstrate that decreasing the substrate lattice constant would increase the minigap size and mass in the transport direction. This leads to reduced quantum tunneling and phonon scattering of the holes. Finally, we illustrate the band-structure modification with substrate lattice constant for other III-V digital alloys. We, thus, provide a recipe for deterministic engineering of sizable valence-band minigaps as a potential recipe for high gain avalanche photodiodes.

DOI: 10.1103/PhysRevB.106.035301

I. INTRODUCTION: THE POTENTIAL IMPACT OF MINIGAPS ON AVALANCHE PHOTODIODE DESIGN

The fields of silicon photonics, telecommunication and light imaging, detection and ranging systems are undergoing unprecedented growth with the emergence of the internet of things, spawning a correspondingly increased demand for efficient photodetectors [1–8]. The avalanche photodiode (APD) is an ideal candidate for such applications due to its intrinsic gain mechanism which enables higher sensitivity [9]. However, the gain performance of an APD is associated with excess noise which arises due to the stochastic nature of the impact ionization process. The excess noise factor $F(M)$ is set by the variance in particle count $\sigma_m^2 = \langle m^2\rangle - \langle m\rangle^2$ vs the mean particle gain $\langle m\rangle = M$ through the relation $\sigma_M^2/M^2 = F(M) - 1 = (M-1)/M + k(M-1)^2/M$. The average particle strength $\langle m^2\rangle$, in turn, contributes to the shot-noise current fluctuation $\langle i_{\text{shot}}^2\rangle = 2qIM^2F(M)\Delta f$ [10–12] for uncorrelated electrons. Here, q is the electron charge, I is the total photo plus dark current, M represents the average multiplication gain, and Δf gives the bandwidth. The excess noise can be minimized by reducing the ratio k of the hole ionization coefficient β to the electron ionization coefficient α for electron injected APDs. For hole-injected APDs the ratio is reversed. Primarily, we can reduce the excess noise in three possible ways—choosing semiconductor materials with favorable impact ionization coefficients, adjusting the multiplication region width to utilize the nonlocal aspect of impact ionization and designing heterojunctions in order to engineer the impact ionization process [9].

Recently, III-V digital alloy APDs with very low excess noise and high gain-bandwidth product operating in the short-infrared wavelength spectrum have been reported [13–15]. Digital alloys are short-period superlattices that include alternately stacked binary compounds in a periodic fashion. The low k in these few digital alloys can be ascribed to multiple factors—the generation of minigaps in the material valence band, a corresponding enhanced valence-band effective mass and finally a large separation between the light-hole and the split-off bands [16–19]. These properties prevent holes from gaining energy and keep them localized near the valence-band edge. However, in these electron-injected APDs, the electrons in the conduction band can easily move to higher energies, bypassing the conduction-band minigaps in order to impact ionize due to their low effective mass.

Minigaps are seen to arise naturally in the first-principles unfolded band structures calculated for the superlattice stack. However, their chemical origin is not well understood and require an in-depth analysis. In Ref. [19], we established that minigaps play a crucial role in limiting hole impact ionization in some III-V digital alloys, particularly, InAlAs, that lead to low excess noise. A sizable minigap prevents transport across it by quantum tunneling and optical phonon scattering processes, thus, restricting them near the valence-band edge. This leads to a reduced hole ionization coefficient and the resulting large asymmetry with the electron ionization coefficient brings about the low excess noise. Whereas the presence

*sza9wz@virginia.edu

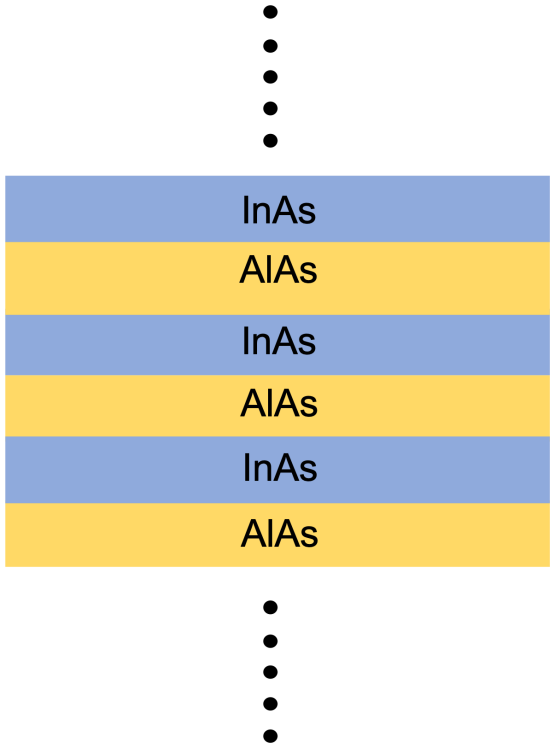

FIG. 1. The schematic of a typical ternary InAlAs digital alloy structure. Here, the InAs and AlAs layers are stacked alternately in a periodic manner.

of minigaps is not a necessary condition for high photogain with low excess noise, it may well prove to be a sufficient condition in many cases. It is, thus, useful to identify ways to engineer such minigaps deterministically with various design knobs, such as alloying and strain.

In this paper, we illustrate the role of strain and its consequent effects on the digital alloy bonding chemistry, that leads to the formation of minigaps. We draw elements from the well-known and simple sp^3 tight-binding model [20,21] to perform this analysis. To perform a detailed analysis, we then employ a more elaborate environment-dependent tight-binding (EDTB) model [22,23] with band unfolding techniques [24–26] to investigate the role of strain in the formation and modulation of these digital alloy minigaps. Furthermore, we study the relationship between biaxial strain and minigap size and their overall impact on carrier transport. This paper provides a convenient design principle towards efficient photodetectors and for overall tunability of electron wave function in digital superlattices.

II. SIMULATION METHOD

A. Environment-dependent tight binding and band unfolding for an atomistic description

A digital alloy (see Fig. 1) band structure requires particular attention to two multiscale attributes—short-range atomistic modifications at the heterointerfaces and long-range band modulation by the superlattice potential. Conventional tight-binding models are typically not suitable for handling the material chemistry at interfaces and surfaces as they are calibrated to the higher-order symmetry of the bulk crystallographic point group [23]. One alternative is to use nonorthogonal tight-binding approaches, such as extended Hückel theory with explicit atomic basis sets, generating parameters that are transferrable between diverse environments, such as bulk vs severely strained and reconstructed surfaces [27,28]. As an alternate, the tight-binding parameters of our EDTB model are explicitly environment dependent, calibrated to state-of-the-art hybrid density functional theory [29] band structure as well as their orbital-resolved wave functions. As a result, the model is able to accurately capture changes due to effects, such as strain and interface reconstruction by tracking changes in the atomic coordinates, bond lengths, and angles. Unstrained and strained bulk III-V materials as well as select alloys were used as fitting targets for the model calibration. In the past, we have demonstrated that our model matches bulk, strained layer and superlattice band structures generated using hybrid functionals [22,30].

Whereas atomistic details are captured by our EDTB, we still have to deal with the large unit cells of our digital alloys, which generate an aggressively scaled Brillouin zone (BZ) and a very complicated band structure due to the proliferation of a large number of zone-folded bands [30]. The sphagettilike band structure is simplified by employing a band-unfolding technique [24–26]. In this method, the supercell bands are projected onto the Brillouin zone of a primitive cell with weights set by decomposing individual eigenfunctions into several Bloch wave functions with separate wave vectors of the primitive cell Brillouin zone. The eigenvector of the supercell $|\vec{K}m\rangle$ can be written as a linear combination of primitive cell eigenvectors $|\vec{k}_i n\rangle$. Additionally, the atomic eigenstate E_p for wave-vector k is represented as a linear combination of atomic-orbital wave functions. The supercell wave-function $|\psi^{\mathrm{SC}}_{m\vec{K}}\rangle$ can be then denoted as a linear combination of primitive cell electron wave functions as [13]

$$\begin{aligned} \left|\psi^{\mathrm{SC}}_{m\vec{K}}\right\rangle &= \sum_n a(\vec{k}_i, n; \vec{K}, m)\left|\psi^{\mathrm{PC}}_{n\vec{k}_i}\right\rangle, \\ \vec{k}_i &\in \{\vec{\tilde{k}}_i\}, \end{aligned} \tag{1}$$

where the electron wave function for the wave-vector $\vec{k}_i$ in the nth band of the primitive cell is represented by $|\psi^{\mathrm{PC}}_{n\vec{k}_i}\rangle$. The supercell and primitive cell reciprocal vectors are designated as $\vec{K}$ and $\vec{k}$, respectively. The folding vector $\vec{G}_{\vec{k}\to\vec{K}}$ containing the projection relationship is written as

$$\vec{K} = \vec{k} - \vec{G}_{\vec{k}\to\vec{K}}. \tag{2}$$

The projection of the supercell wave-function $|\psi^{\mathrm{SC}}_{m\vec{K}}\rangle$ into the primitive cell wave-function $|\psi^{\mathrm{PC}}_{n\vec{k}_i}\rangle$ is denoted by

$$P_{m\vec{K}} = \sum_n \left|\left\langle\psi^{\mathrm{SC}}_{m\vec{K}}\middle|\psi^{\mathrm{PC}}_{n\vec{k}_i}\right\rangle\right|^2. \tag{3}$$

A pristine image of the band evolution from the individual primitive components to the superlattice bands can be obtained by plotting these projection coefficients. The EDTB model together with the band-unfolding tool are used to compute the band structures in the subsequent Results and Discussion section.

B. Nonequilibrium Green's-function method for coherent transmission

When it comes to simulating carrier transport, it is worth keeping in mind that there are two primary mechanisms by which carriers can bypass the minigaps, namely, quantum tunneling and optical phonon scattering. The impact of tunneling through a minigap is readily captured by computing the ballistic transmission in three-dimensional (3D) using the nonequilibrium's Green's-function (NEGF) formalism [31]. For this purpose, we developed a NEGF model that utilizes the Hamiltonian obtained from the EDTB model. The digital alloys are translationally invariant on the plane perpendicular to the growth direction, whereas having finite nonperiodic hopping in the growth (transport) direction. The 3D Hamiltonian is broken into nearest-neighbor blocks, including the applied electric field, in the real-space basis along the transport z direction, whereas Fourier transforming in the transverse x-y directions, in the k-space basis to capture in-plane structural periodicity. This results in a Hamiltonian of the form $H(r_z, k_x, k_y)$. We start with the 3D EDTB Hamiltonian whose matrix elements are in symmetrically orthogonalized atomic orbital basis $|nb\mathbf{R}\rangle$. Here, the atom position is denoted by $\mathbf{R}$, the orbital type (s, p, d, or s^*) is given by n and b represents the atom type (cation or anion). The full Fourier transformation of this real-space Hamiltonian results in the elements being represented in the k-space basis $|nb\mathbf{k}\rangle$. This 3D Hamiltonian is converted into a position-dependent (along growth direction) quasi-one-dimensional (-1D) Hamiltonian by performing a partial Fourier transform in the basis $|nbj\mathbf{k}_\parallel\rangle$ with "parallel" momentum $\mathbf{k}_\parallel = (k_x, k_y)$ and "perpendicular" positions $x_j = a_L/4$ [19,32,33],

$$|nbj\mathbf{k}_\parallel\rangle = L_{\mathrm{BZ}}^{-1/2} \int dk_z e^{-ik_z j a_L/4} |nb\mathbf{k}\rangle. \tag{4}$$

Here, the length of the 1D Brillouin-zone $L_{\mathrm{BZ}} = 8\pi/a_L$, over which the k_z integral is performed. The distance between nearest-neighbor planes is one-fourth the lattice constant a_L in a zinc-blende crystal resulting in $x_j = a_L/4$. The accurate EDTB Hamiltonian offers significant advantages over conventional DFT Hamiltonians that have well-known issues with derivative discontinuity, orbital-independent functionals, overbinding and quantitatively poor fitting of bulk semiconducting band gaps (resolved to some degree with hybrid functionals), but above all require significantly heavier computational power.

At the two ends of the digital alloy device, we consider extensions of the same material at constant potential as contacts, generating a semiperiodic array of transport blocks with on-site matrix $\alpha_{i\vec{k}_\parallel}$ ($i = 1, 2$ for the bias-separated contacts at the two ends) and hopping matrix $\beta_{\vec{k}_\parallel}$. Using recursion, we find the two contact surface Green's-functions g and then the self-energy matrices Σ, whose anti-Hermitian parts give us the broadening matrices Γ related to the electron escape rates into the contacts,

$$\begin{aligned} g_{1\vec{k}_\parallel}^{-1} &= \alpha_{1\vec{k}_\parallel} - \beta_{\vec{k}_\parallel}^\dagger g_{1\vec{k}_\parallel} \beta_{\vec{k}_\parallel}, \quad & \Sigma_{1\vec{k}_\parallel} &= \beta_{\vec{k}_\parallel}^\dagger g_{1\vec{k}_\parallel} \beta_{\vec{k}_\parallel}, \\ g_{2\vec{k}_\parallel}^{-1} &= \alpha_{2\vec{k}_\parallel} - \beta_{\vec{k}_\parallel} g_{1\vec{k}_\parallel} \beta_{\vec{k}_\parallel}^\dagger, \quad & \Sigma_{2\vec{k}_\parallel} &= \beta_{\vec{k}_\parallel} g_{2\vec{k}_\parallel} \beta_{\vec{k}_\parallel}^\dagger, \\ \Gamma_{i\vec{k}_\parallel} &= i(\Sigma_{i\vec{k}_\parallel} - \Sigma_{i\vec{k}_\parallel}^\dagger). \end{aligned} \tag{5}$$

We can then calculate the retarded Green's-function G and the quantum-mechanical transmission T using the Fisher-Lee formula [31],

$$\begin{aligned} G_{\vec{k}_\parallel}(E) &= [(E + i0^+)I - H_{\vec{k}_\parallel} - \Sigma_{1\vec{k}_\parallel} - \Sigma_{2\vec{k}_\parallel}]^{-1}, \\ T &= \sum_{\vec{k}_\parallel} \mathrm{Tr}(\Gamma_{1\vec{k}_\parallel} G_{\vec{k}_\parallel} \Gamma_{2\vec{k}_\parallel} G_{\vec{k}_\parallel}^\dagger). \end{aligned} \tag{6}$$

The energy-resolved net current density from the layer m to layer $m+1$ is expressed as [32]

$$\begin{aligned} J_{m,m+1}(E) = -\frac{iq}{h} \int \frac{\mathbf{k}_\parallel}{(2\pi)^2} \mathrm{Tr}[&G_{m+1,m}^{n,p} H_{m,m+1} \\ &- G_{m,m+1}^{n,p} H_{m+1,m}]. \end{aligned} \tag{7}$$

The tight-binding hopping element between layers m and $m+1$ along the transport/growth direction is denoted by $H_{m,m+1}$ in Eq. (7). Here, electron (n) and hole (p) densities are represented by $G^n = G\Sigma^{\mathrm{in}}G^\dagger$ and $G^p = G\Sigma^{\mathrm{out}}G^\dagger$, correspondingly. The in-scattering function $\Sigma^{\mathrm{in}} = \Gamma_1 f_1 + \Gamma_2 f_2$ and the out-scattering function $\Sigma^{\mathrm{out}} = \Gamma_1(1 - f_1) + \Gamma_2(1 - f_2)$, where $f_{1,2}$ are the Fermi-Dirac distributions at the contacts. These aforementioned quantities are all in the basis of $k_\parallel$. Using this model, we compute the energy-dependent ballistic transmission to see how minigap size impacts the quantum tunneling process.

C. Boltzmann transport model for incoherent scattering

Including phonon scattering in NEGF typically requires generalizing from Fisher-Lee to the Meir-Wingreen incoherent transport formulation with an added phonon self-energy obtained within the self-consistent Born approximation [31]. Instead, we study the effect of phonon scattering in the digital alloys using a multiband Boltzmann transport model that focuses on classical transport with the quantum physics hidden in the band parameters. The model outputs the energy-resolved carrier occupation probability, which we calculate to explore the effect of minigaps on phonon scattering.

Under the influence of an external electric field, the digital alloy carriers do not follow the standard Fermi-Dirac distribution but rather redistribute themselves in real and momentum space. We employed a multiband Boltzmann transport equation model to compute the modified digital alloy carrier distribution,

$$\begin{aligned} \vec{v} \cdot \nabla_{\mathbf{r}} f_n + \vec{F} \cdot \nabla_{\mathbf{k}} f_n = &\sum_{m,\vec{p}'} (\vec{p}', \vec{p}) f_m(\vec{p}')[1 - f_n(\vec{p})] \\ &- \sum_{m,\vec{p}'} S(\vec{p}, \vec{p}') f_n(\vec{p})[1 - f_m(\vec{p}')]. \end{aligned} \tag{8}$$

In the equation, the carrier distribution is $f = f(\mathbf{r}, \mathbf{k})$ with n and m representing band indices, $\vec{p}$ and $\vec{p}'$ are the momenta of the carriers, and the scattering rate is $S(\vec{p}', \vec{p})$. The ballistic trajectory in phase space under the applied field is described by the left side of the equation. The right-hand side denotes the intraband and interband scattering processes. For our simulations, we consider a homogeneous system with a constant electric field. As a result, we can assume $\nabla_{\mathbf{r}} f = 0$ since the distribution function becomes independent of position.

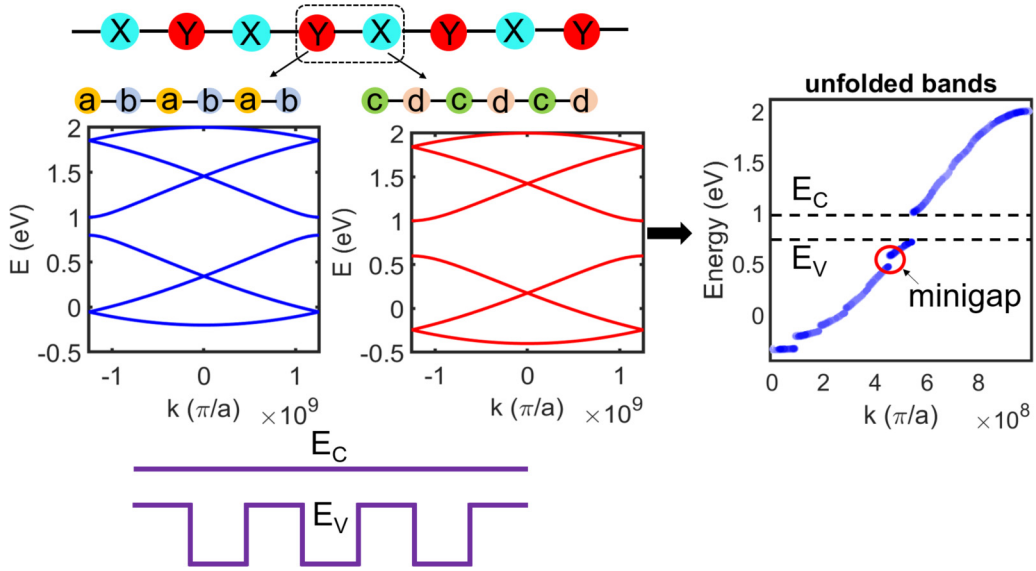

FIG. 2. In a toy model, we consider a unit cell (dotted box) consisting two arbitrary binary materials. By adjusting their on-site energies and hopping parameters a material system with zero conduction-band offset and large valence-band offset is created. The large valence-band offset results in the formation of a small gap called a minigap in the valence band (within red circle) as shown in the unfolded band structure. There are no prominent conduction-band minigaps due to zero band offset.

In an APD, optical phonon scattering is the alternate method for overcoming minigaps besides tunneling. The optical phonon scattering $S(\vec{p}', \vec{p})$ for a phonon energy $\hbar\omega_{opt}$ is expressible in terms of Fermi's golden rule,

$$S(\vec{p}', \vec{p}) = \frac{2\pi}{\hbar}|H_{\vec{p},\vec{p}'}|^2\delta_{\vec{p}',\vec{p}\pm\vec{\beta}}\delta[E(\vec{p}') - E(\vec{p}) \pm \hbar\omega_{opt}]. \quad (9)$$

The digital alloy band-structures $E(\vec{p})$ and $E(\vec{p}')$ are calculated using the EDTB model. The constant effective scattering strength $H_{\vec{p},\vec{p}'}$ is extracted from experimental mobility $\mu = q\tau/m^*$. Here, m^* is the carrier effective mass and τ is the scattering lifetime, which is essentially $1/S(\vec{p}', \vec{p})$. A more detailed description of the calculation of $H_{\vec{p},\vec{p}'}$ is provided in Ref. [19].

III. A TOY MODEL: ORIGIN OF VALENCE-BAND MINIGAPS

Previous studies of digital alloys, such as InAlAs, AlInAsSb, and AlAsSb [13,16–18] have demonstrated that valence-band minigaps present in the material band structure play a part in reducing excess noise by limiting hole carrier transport. However, the role of minigap is firmly established for one material combination InAlAs [19]. For the other materials either a systematic experimental comparison between digital and random alloy superlattices does not exist, or when it does, the random shows low noise as well and is attributed to an energy separated split-off band [19]. Nonetheless, a deterministic creation of a strong minigap can significantly aid APD gain by suppressing one carrier type. In this section, we explore the formation of these gaps using a one-dimensional simple toy model.

We consider an arbitrary alloy consisting of two materials X and Y stacked alternately, such as a digital alloy as shown in Fig. 2. Each of these materials is essentially a dimer consisting of a set of two atoms. For X, the component atoms are a and b, and for Y they are c and d. The resulting Hamiltonian of the unit cell for this material then looks, such as,

$$H = \begin{pmatrix} \alpha_X & -\beta_X & & & & -\gamma_{YX1} \\ -\beta_X^\dagger & \alpha_X & -\beta_X & & & \\ & -\beta_X^\dagger & \alpha_X & -\gamma_{XY1} & & \\ & & -\gamma_{XY2} & \alpha_Y & -\beta_Y & \\ & & & -\beta_Y^\dagger & \alpha_Y & -\beta_Y \\ -\gamma_{YX2} & & & & -\beta_Y^\dagger & \alpha_Y \end{pmatrix}, \quad (10)$$

where

$$\alpha_X = \begin{pmatrix} E_X & -t_1 \\ -t_1 & E_X \end{pmatrix}, \quad \beta_X = \begin{pmatrix} 0 & 0 \\ t_2 & 0 \end{pmatrix}, \quad (11)$$

$$\alpha_Y = \begin{pmatrix} E_Y & -t_3 \\ -t_3 & E_Y \end{pmatrix}, \quad \beta_Y = \begin{pmatrix} 0 & 0 \\ t_4 & 0 \end{pmatrix}, \quad (12)$$

$$\gamma_{XY1} = \begin{pmatrix} 0 & 0 \\ t_5 & 0 \end{pmatrix}, \quad \gamma_{XY2} = \begin{pmatrix} 0 & t_6 \\ 0 & 0 \end{pmatrix}, \quad (13)$$

$$\gamma_{YX1} = \begin{pmatrix} 0 & t_7 \\ 0 & 0 \end{pmatrix}, \quad \gamma_{YX2} = \begin{pmatrix} 0 & 0 \\ t_8 & 0 \end{pmatrix}. \quad (14)$$

For each material, we consider the on-site energies, $E_{X,Y}$ to be constant, whereas the hopping parameters t_{1-4} between the dimer elements vary. t_{5-8} represent the coupling between material X and material Y. Here, we set $E_X = 0.9$, $E_Y = 0.8$, $t_1 = 0.6$, $t_2 = 0.5$, $t_3 = 0.7$, $t_4 = 0.5$, $t_5 = -0.4$, $t_6 = -0.6$, $t_7 = -0.4$, and $t_8 = -0.6$ in eV. These parameter values are chosen such that there is a large valence-band offset between X and Y but the conduction-band offset is zero as depicted in Fig. 2. The resulting unfolded band structure is shown on the right side of the figure. We observe that a clear minigap forms in the valence band (highlighted with a red circle), whereas correspondingly large minigaps do not arise in the conduction band.

This simple example illustrates that sizable minigaps can be engineered selectively in one band with large on-site

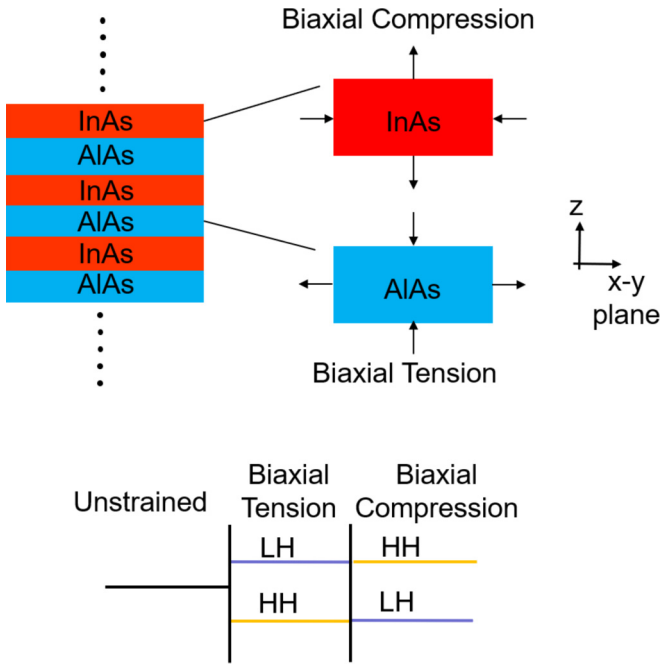

FIG. 3. Six-monolayer (ML) InAlAs consists of InAs and AlAs grown on an InP substrate. With respect to the InP lattice constant a_{InP}, the InAs lattice constant a_{InAs} $a_{\mathrm{InAs}} > a_{\mathrm{InP}}$ and the AlAs lattice constant $a_{\mathrm{AlAs}} < a_{\mathrm{InP}}$. Thus, InAs experiences biaxial compression, and AlAs experiences biaxial tension. Biaxial strain results in splitting the HH and LH bands. Since InAs and AlAs experience opposite kinds of strain, their bands move in opposite directions, ensuing a large valence-band offset. This opens minigaps in the InAlAs valence band.

energy variations in the frontier atomic orbitals that generate that band. We will now explore how such large offsets can be deliberately and selectively engineered in one band in the III-V digital alloys using strain.

IV. RESULTS AND DISCUSSION

In bulk heterojunctions, band discontinuities form at the interface owing to the alignment of Fermi levels of the constituent components, resulting in band offsets. The band offset sizes can be manipulated if the position of band edges can be altered [34]. This is achieved by means of hydrostatic pressure [35], applying biaxial strain [36–40], and alloying [41,42]. In digital alloys it is biaxial strain that results in the opening of the minigaps as we will describe next.

It is well known that biaxial strain in semiconductors removes the degeneracy of the valence bands and results in the splitting of the heavy-hole (HH) and light-hole (LH) bands [42,43]. Let us consider the case of InAlAs to understand how minigaps form. In Fig. 3, it is shown that InAlAs consists of InAs and AlAs stacked alternately. The alloy is grown on an InP substrate having a lattice constant 5.87 Å [22]. Compared to InP, the lattice constant of InAs at 6.06 Å is greater wheereas that of AlAs at 5.66 Å is smaller. As a result, AlAs experiences biaxial tension on the x-y plane, whereas InAs undergoes biaxial compression. In the (001) z direction, InAs undergoes expansion, and AlAs undergoes compression. As we detail in the Appendix, biaxial tension results in LH

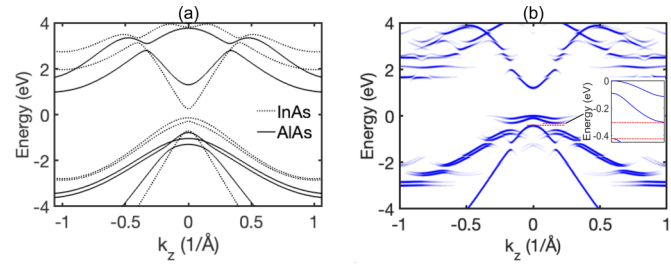

FIG. 4. (a) Band structure of InAs and AlAs grown on an InP substrate, (b) unfolded band structure of six-ML InAlAs with InP as the substrate. The band structures above are calculated using the $sp^3s^*d^5$ EDTB model. Here, at a wave-vector k_z, the color density represents the probability of a supercell state projecting onto this primitive cell state. Around the Γ point ($k_z = 0$) in (a) there is a large band offset between the InAs and the AlAs bands. Consequently, in (b) we observe minigaps in the InAlAs valence band around the Γ point. A zoomed view of the minigap is provided in the inset of (b).

bands moving up and HH moving down in energy, depicted at the bottom of Fig. 3. The opposite happens for biaxial compression. As the bands in the alternately strained layers move in opposite directions, the band offset increases, resulting in the formation of the minigaps.

Figure 4(a), shows the band structure of the strained InAs and AlAs (grown on the InP substrate) computed with the $sp^3s^*d^5$ EDTB model [22]. We observe a large valence-band offset at the Γ point between the strained AlAs and the InAs. The unfolded band structure of a six-monolayer InAlAs showing the resulting valence-band minigaps, computed with the EDTB model, is depicted in Fig. 4(b). The unit cell of the InAlAs DA considered consists of three-ML AlAs and three-ML InAs.

A short visual synopsis of the chemical origin of strain-induced migration of valence bands is presented in Fig. 5. In short, compressive strain along a cubic axis rotates and reduces overlap among frontier orbitals responsible for LH bands along that axis, decreasing their antibonding split and raising LH bands in energy. Simultaneously, they increase orbital overlaps responsible for HH bands and push down those bands in energy. In the Appendix, we deconstruct the separate movement of LH and HH bands in terms of their detailed orbital chemistry in the presence of strain. These results are illustrated in detail in the Appendix, following well-established arguments using sp^3 tight-binding models. The EDTB model we use to calculate digital alloy band structures incorporates higher-order orbital interactions in an inhomogeneous environment. However, the qualitative physics for strain-induced band migration and eventually minigap formation remains the same.

Having a detailed understanding of the underlying physics of the minigaps, it is then useful to see how we can control the minigap size in these digital alloys by tracking their band evolution under strain. We compute the band structure for two cases: contraction—the substrate lattice constant is smaller than that of the active APD material (InP for InAlAs), and expansion—in which the substrate lattice is greater. The band structures for strained InAs and AlAs under contraction and expansion are shown in Figs. 6(a) and 6(b). Under these

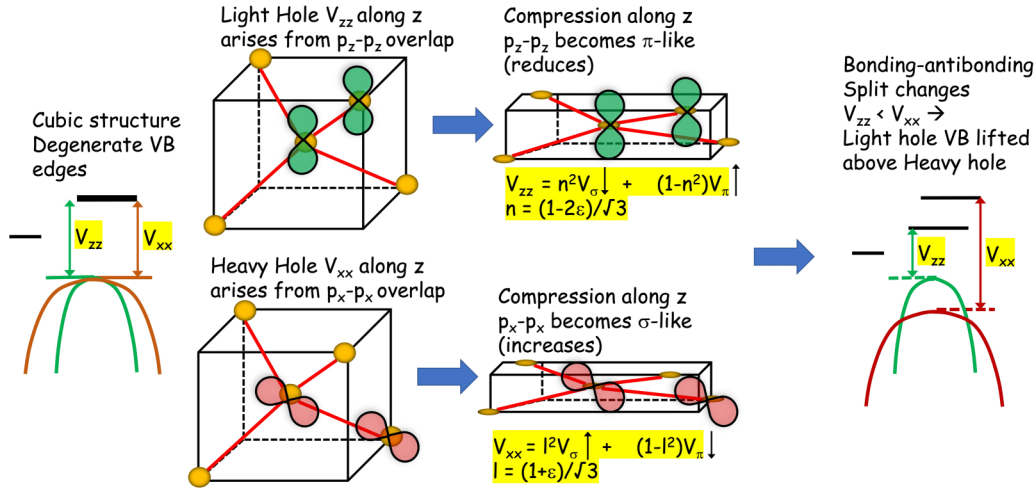

FIG. 5. (Left) Degenerate valence-band edges in zinc-blended structures are created by degenerate antibonding splittings with light holes along the z axis created by overlap of p_z bonds and heavy orbitals by transverse $p_{x,y}$ orbitals. Upon compressive strain along the z axis (middle), the orbitals rotate around the center of the unit cell, becoming more edge on (π like) for p_z light holes with reduced overlap and antibonding split, and more head on (σ like) for $p_{x,y}$ orbitals with increased overlap and antibonding split. The end result is LH bands are pushed up and HH bands are pushed down, breaking the cubic degeneracy of the valence bands at the Γ point. The opposite happens for a tensile strain.

conditions, the binary constituents experience unequal biaxial strains and due to their different Poisson ratios D_{001} also undergo different strains in the z direction. Thus, their valence bands move by different amounts. InAs has a higher D_{001} than AlAs [38], and, hence, bands of InAs are more responsive to strain. We note that the valence-band offset under contraction is large compared to expansion case. Consequently, the valence bands of InAlAs under contraction become flatter, and the minigaps increase in size as depicted in Fig. 6(c). However, we can see in Fig. 6(d) that under expansion the InAlAs top valence-band effective mass decreases, and the minigaps become smaller.

The 2D energy contours of the top InAlAs band on the x-y plane are shown in Fig. 7 for regular, contracted, and expanded cases. We observe that for the regular and contraction cases, the top bands are highly anisotropic. Under biaxial strain, in the in-plane (x and y) directions the bands move in the opposite direction to that of the out-of-plane (z) direction [43]. As a result, under contraction the effective mass on the x-y plane decreases. Comparing Fig. 7(b) with Fig. 7(a), we observe the contour lines become more elliptical which indicates the lowering of the mass under contraction. The effective mass increases for expansion as the contour lines becomes flatter in Fig. 7(c). This observed anisotropic nature of the bands can be utilized to explore the use of digital alloys, such as InAlAs in other applications, such as transistors.

One key aspect we need to study is the impact of the strain on carrier transport of digital alloys. Since we have been

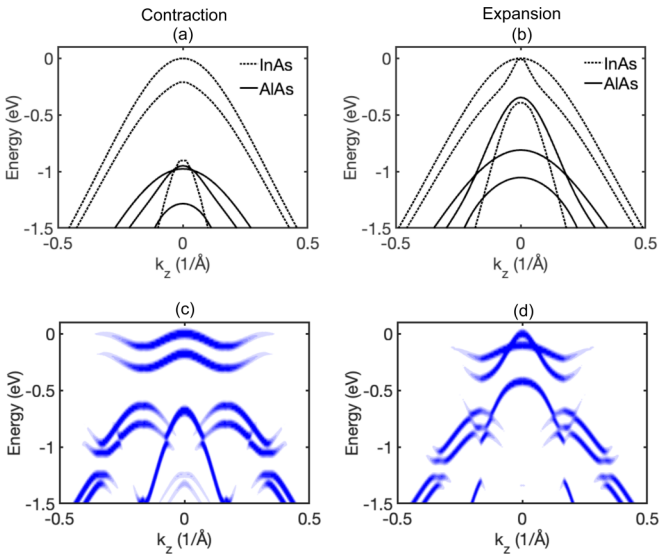

FIG. 6. Band structure of strained InAs and AlAs for (a) "contraction"—where the substrate lattice constant is 3% less than the InP lattice constant and (b) the expansion—substrate lattice constant is 3% more than the InP lattice constant. The unfolded band structure of six-ML InAlAs under contraction and expansion is shown in (c) and (d), respectively. Contraction results in a larger valence-band offset around the Γ point in (a) whereas expansion causes the valence-band offset to decrease in (b). As a result, there are larger valence-band minigaps in (c) and smaller minigaps in (d), respectively.

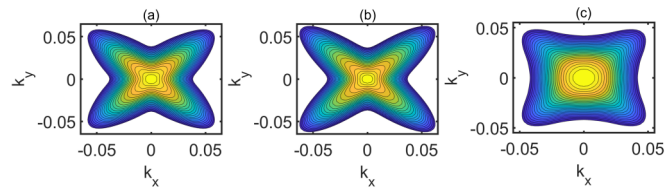

FIG. 7. Two-dimensional energy contour on the x-y plane of the top band of InAlAs for (a) regular, (b) contraction, and (c) expansion. The energy range for the contour is from 0.025 to 0.5 eV below the valence-band edge. On the transverse plane, the effective mass decreases due to contraction as seen in the more elliptical shape in (b). In (c), the flatter contour lines represent an increase in effective mass on the transverse plane. The biaxial strain is an effective tuning knob for the asymmetric band structure of the digital alloys.

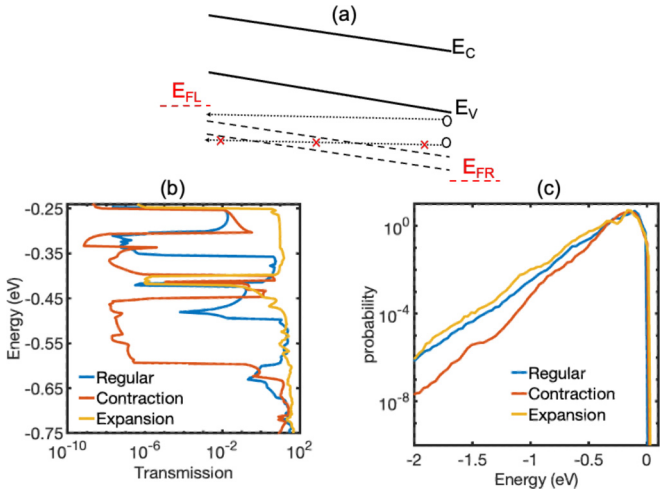

FIG. 8. (a) Band-edge diagram of the digital alloy considered. A minigap act as a barrier to hole transport in the digital alloy valence band. A large minigap cannot be bypassed by intraband tunneling or optical phonon scattering processes, thus, limiting the holes near the valence-band edge. (b) Ballistic transmission vs energy and (c) carrier occupation probability vs energy in the valence band for six-ML InAlAs with regular, compressive, and tensile strains.

primarily concerned with the effect of strain in the valence bands, we look at the effect on carrier transport in the InAlAs valence band in Fig. 8. The effect of minigaps on digital alloy valence-band carrier transport is shown in the band diagram of Fig. 8(a). Here, the region between the dotted lines represent the minigap. In the absence of a minigap the holes can easily accelerate under bias and gain sufficient energy to impact ionize as shown by the hole near the valence-band edge. The minigap act as a barrier to carrier transport and can be bypassed by quantum tunneling or optical phonon scattering. A sufficiently large minigap prevents transport by these processes. As a result, holes are restricted near the valence-band edge, and their impact ionization is prevented. The resulting asymmetry between the electron and the hole ionization coefficient makes the APD gain more deterministic, thus, reducing APD excess noise. Figure 8(b) depicts the ballistic transmission vs energy spectrum in the valence band under regular, expansion, and contraction conditions in six-ML InAlAs, under an applied bias of 0.25 V. The transmission has been computed using the NEGF formalism described earlier. In order to study the effect of minigaps on intraband tunneling, we set the quasi-Fermi level of the left contact E_{FL} at -0.25 eV below the valence-band edge and quasi-Fermi level of the right contact E_{FR} at another -0.25 eV below. The reference point 0 eV is the valence band of the left contact. The material for the contacts is same as the channel material, i.e., InAlAs DA. We observe that as we go from expansion to regular to contraction case the transmission gaps increase in size due to increasing size of the minigaps and enhanced effective mass. As a result, the probability to tunnel across the minigaps decreases, and the holes become more localized near the valence band. This will help in reducing the excess noise in APDs. Another mechanism by which holes can bypass the minigaps is optical phonon scattering. We look at the effect of this scattering using the Boltzmann transport equation. The carrier probability vs energy with optical phonon scattering under an electric field of 1 MV/cm is shown in Fig. 8(c). Under the expansion condition, holes have a higher probability to occupy higher-energy states compared to the regular and contraction cases. Under contraction, the probability is the lowest. This is a further confirmation that contraction prevents holes from reaching higher energies. It is then possible to design better low noise electron injected digital alloy APDs with lower hole impact ionization by applying contraction to materials, such as InAlAs.

In addition to InAlAs, we also computed the band structures of six-ML InGaAs, ten-ML AlInAsSb, five-ML AlAsSb, and six-ML AlAsSb digital alloys under regular, contraction and expansion conditions along the 001 direction. These band structures are shown in Fig. 9. The primary binary constituents for these alloys are as follows: InAs and GaAs for InGaAs, InAs and AlSb for AlInAsSb, AlAs, AlSb for AlAsSb, and AlAs and GaAs for AlGaAs. For the regular band structures, InGaAs and AlAsSb have an InP substrate, AlInAsSb has a GaSb substrate, and AlGaAs has a GaAs substrate. The lattice constants for all these materials are taken from the paper by Tan *et al.* [22]. The period thicknesses used for these materials represent the period thicknesses of the corresponding fabricated devices [19]. For InGaAs, AlInAsSb, and AlAsSb one of the binary constituents has a lattice constant that is greater than the substrate lattice constant whereas the other constituent lattice constant is smaller. Thus, the binary components experience alternating types of strain. This is not the case for AlGaAs. For all the material combinations, we observe that the effective mass of the top valence band increases under contraction and reduces for expansion. This is mainly because under contraction HH states move up in energy whereas under expansion they move down leaving LH states as the top states in the valence band. Figure 10 shows the relationship between the minigap size and the substrate lattice is constant. We observe that minigap size decreases with increasing lattice constant. For InGaAs, we see that the minigap increases in size with contraction from 0.03 to 0.16 eV which is similar to the behavior of InAlAs described earlier. In AlInAsSb there is a separation between the HH and the LH bands around the Γ point under contraction. A similar gap is seen for AlAsSb under the regular condition. This gap size increases under contraction. The gaps vanish for both AlInAsSb and AlAsSb under expansion. The minigap sizes also increase under contraction by about 0.04 eV for AlInAsSb and 0.02 eV for AlAsSb. However, for AlGaAs we do not observe any minigaps in the light-hole band. This is primarily because the HH/LH bands of the binary constituents in AlGaAs move in the same direction under strain as both experience same type of biaxial strain.

V. CONCLUSION

In this paper, we demonstrated that biaxial strain can be used as a useful tool to control the oscillatory orbital contributions and, thus, the split in degeneracy between LH and HH valence bands, creating sizable minigaps and providing a potential path towards deterministic engineering of digital alloy APDs with low excess noise. As a general rule, we expect that

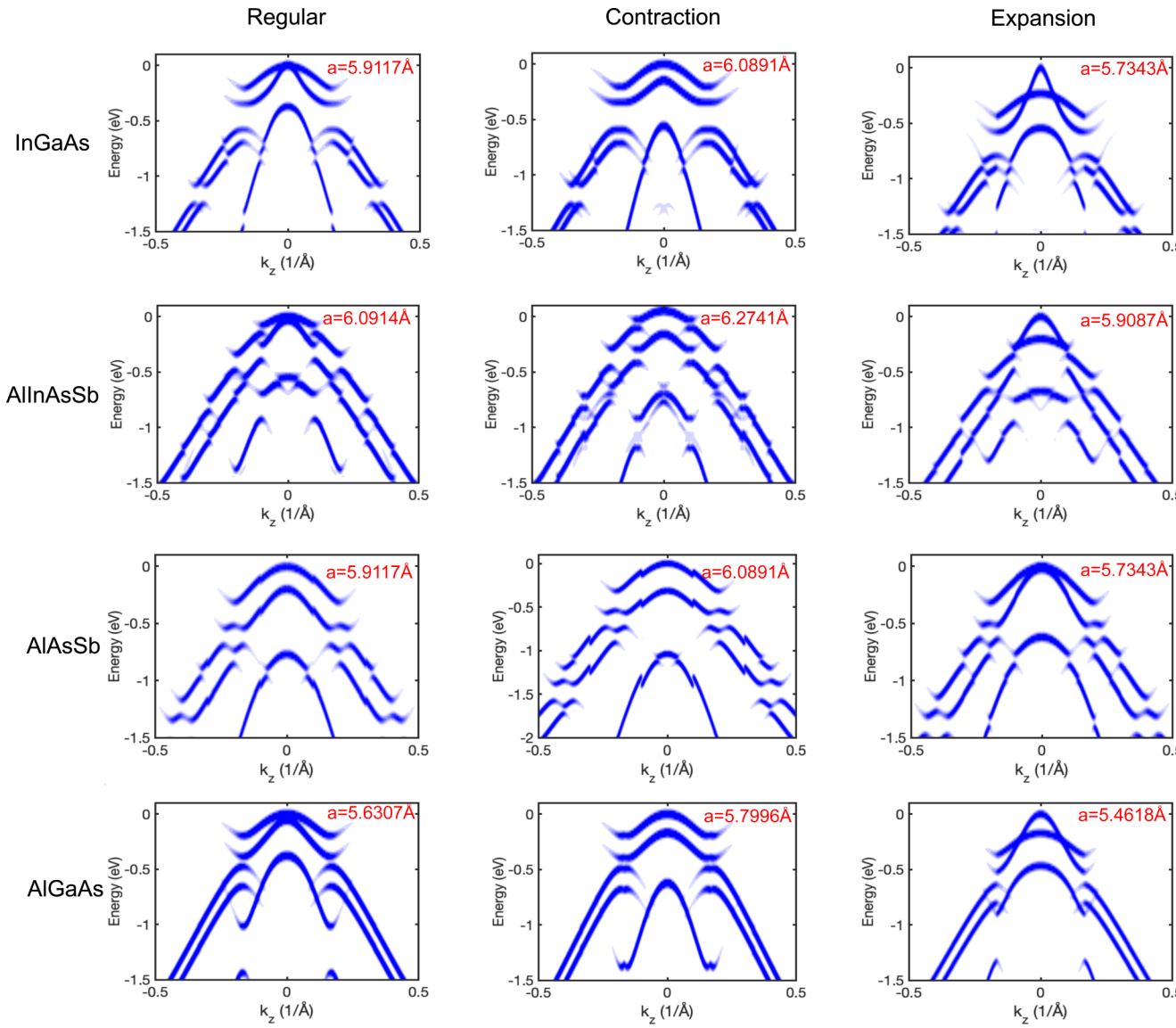

FIG. 9. Band structure of six-ML InGaAs, ten-ML AlInAsSb, five-ML AlAsSb, and six-ML AlGaAs for regular, contraction, and expansion cases. The substrate constant was decreased by 3% and increased by 3%, respectively, for the contraction and expansion cases with respect to the regular case. The regular lattice constant is that of the material used as the substrate in the experimental device. Contraction leads to a larger minigap in the LH band with flatter bands. On the contrary, smaller minigaps and lighter effective mass are generally observed for the expansion cases.

decreasing the substrate lattice constant will increase minigap size that will enhance the performance of digital alloy APDs.

ACKNOWLEDGMENT

This work was funded by National Science Foundation Grant No. NSF 1936016. We thank Dr. J. P David of University of Sheffield and Dr. S. R. Bank of the University of Texas-Austin for important discussions and insights. The calculations are performed using the computational resources from High-Performance Computing systems at the University of Virginia (Rivanna) and the Extreme Science and Engineering Discovery Environment (XSEDE), which is supported by National Science Foundation Grant No. ACI-1548562.

APPENDIX: IMPACT OF STRAIN ON VALENCE-BAND DEGENERACY

In this Appendix, we will elaborate the orbital chemistry underlying strain-induced migration of valence bands in the III-V APD materials. In a bulk zinc-blende semiconductor, each atom is tetrahedrally bonded to four neighboring atoms. The bonds connecting these atoms point toward the ⟨111⟩ directions of the cube that bounds around the tetrahedron. Every bond consists of 25% contribution each from the s, p_x, p_y, and p_z orbitals [43]. The chemical bonds of an unstrained zinc-blende crystal have cubic point group symmetry, so the valence bands are degenerate at the Γ point. However, under biaxial tension (uniaxial compression along z) all the bonds are equally rotated towards the x-y plane, whereas under biaxial compression they move away from the x-y plane. Near

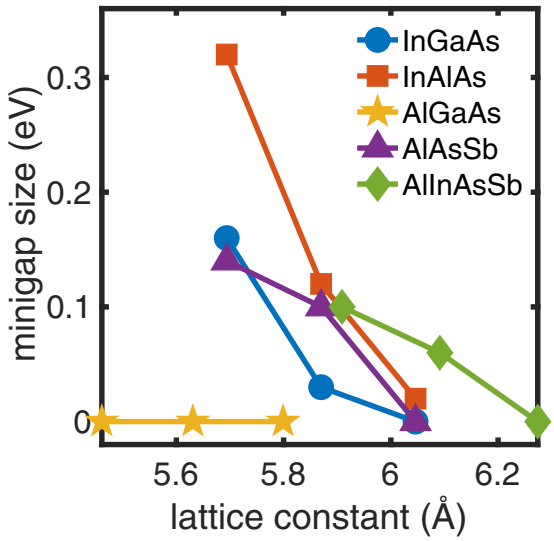

FIG. 10. Minigap size vs substrate lattice constant. A decreasing trend with an increasing lattice constant is observed for all the materials except AlGaAs.

the valence-band edge, bonding states arising from the overlap of the directional frontier p orbitals that dominate formation of the bands there. The spherical s orbitals contribute to the conduction-band edge states. Considering only contributions from the p orbitals and projecting one of the tetrahedral bonds along a principal direction ($\langle 100\rangle$, $\langle 110\rangle$, or $\langle 111\rangle$), the out-of-plane orbital forms the LH states, i.e., p_z orbital along the (001) or z direction. Then, HH states are formed by the in-plane orbitals, for instance, p_x and p_y orbitals, if we are looking from the z direction. We can then explain the effect of strain on these p orbitals using a simple sp^3 tight-binding model. The ignored virtual s^* and d orbitals end up being important quantitatively, the former for indirect band-gap semiconductors, such as Si, the latter to nail down its transverse effective masses. However, they have less qualitative relevance to direct band-gap III-V materials. We use the full $sp^3s^*d^5$ set for our numerical evaluations, but a simplified sp^3 for the current qualitative arguments.

Chadi and Cohen [20] and Harrison [21] used the sp^3 tight-binding model to investigate the electronic band structure of various diamond and zinc-blende crystals. In the model, the valence-band orbitals form the the conduction and valence bands. Each atom in the primitive cell contributes an s, p_x, p_y, and p_z orbital. The resulting Hamiltonian is an 8×8 matrix without inclusion of spin-orbit coupling. At the Γ point, the sp^3 Hamiltonian can be simplified to

$$H=\begin{pmatrix} E_{SC} & V_{SS} & 0 & 0 & 0 & 0 & 0 & 0\\ V_{SS} & E_{SA} & 0 & 0 & 0 & 0 & 0 & 0\\ 0 & 0 & E_{PC} & V_{XX} & 0 & 0 & 0 & 0\\ 0 & 0 & V_{XX} & E_{PA} & 0 & 0 & 0 & 0\\ 0 & 0 & 0 & 0 & E_{PC} & V_{YY} & 0 & 0\\ 0 & 0 & 0 & 0 & V_{YY} & E_{PA} & 0 & 0\\ 0 & 0 & 0 & 0 & 0 & 0 & E_{PC} & V_{ZZ}\\ 0 & 0 & 0 & 0 & 0 & 0 & V_{ZZ} & E_{PA} \end{pmatrix}. \tag{A1}$$

This Hamiltonian can be simplified into four 2×2 matrices representing the overlap between the constituent two atoms of the four different orbitals considered. The eigenstates at the valence-band edge can be computed from the Hamiltonians of the p_x, p_y, and p_z orbitals,

$$H_1=\begin{pmatrix} E_{PC} & V_{XX}\\ V_{XX} & E_{PA}\end{pmatrix},\quad H_2=\begin{pmatrix} E_{PC} & V_{YY}\\ V_{YY} & E_{PA}\end{pmatrix}, \tag{A2}$$

$$H_3=\begin{pmatrix} E_{PC} & V_{XX}\\ V_{XX} & E_{PA}\end{pmatrix}. \tag{A3}$$

Here, $E_{A,C}$ represents the on-site energy of the anion and cation, respectively, and V_{ii} is the interaction constant representing the orbital overlap. The valence-band states at the Γ point can be computed by diagonalizing these matrices to get

$$\begin{aligned} E_1&=\frac{E_{PC}+E_{PA}}{2}-\sqrt{\left(\frac{E_{PC}-E_{PA}}{2}\right)^2+V_{XX}^2},\\ E_2&=\frac{E_{PC}+E_{PA}}{2}-\sqrt{\left(\frac{E_{PC}-E_{PA}}{2}\right)^2+V_{YY}^2},\\ E_3&=\frac{E_{PC}+E_{PA}}{2}-\sqrt{\left(\frac{E_{PC}-E_{PA}}{2}\right)^2+V_{ZZ}^2}. \end{aligned} \tag{A4}$$

For an unstrained system $V_{XX}=V_{YY}=V_{ZZ}$, which results in degenerate bands. This is consistent with the observation that bulk semiconductors are symmetric along all the cubic axes. Each p orbital bond consists of head-on (σ) and side-on (π) couplings. The interaction constant V_{ii} is written in terms of contributions from these bonds. θ represents the azimuthal angle between the bond and the relevant axis for the constant we are considering, i.e., x axis for V_{XX}. These interaction constants can be written in terms of the directional consines (l,m,n) [44],

$$\begin{aligned} V_{XX}&=l^2V_{pp\sigma}+(1-l^2)V_{pp\pi},\\ V_{YY}&=m^2V_{pp\sigma}+(1-m^2)V_{pp\pi},\\ V_{ZZ}&=n^2V_{pp\sigma}+(1-n^2)V_{pp\pi}. \end{aligned} \tag{A5}$$

For an unstrained system, $(l,m,n)=(1,1,1)/\sqrt{3}$ resulting in $V_{XX}=V_{YY}=V_{ZZ}$ and, hence, degenerate energy levels at the valence-band edge.

The strain tensor of a system can be broken down into three components—a hydrostatic strain and two kinds of shear strain [34]. The hydrostatic strain results in overall shifting of the energy bands as the crystal symmetry is not broken. However, biaxial shear strain results in the breaking of crystal symmetry, lifting band degeneracy at the Γ point and resulting in band warping as well. Under biaxial strain on the x-y plane, the traceless shear strain tensor can be written as

$$\frac{1}{3}\begin{pmatrix} e_{xx}-e_{zz} & 0 & 0\\ 0 & e_{xx}-e_{zz} & 0\\ 0 & 0 & -2(e_{xx}-e_{zz})\end{pmatrix}, \tag{A6}$$

where $e_{xx}=a_\parallel/a_i-1$ and $e_{zz}=-D_{001}e_{xx}$. Here, $a_\parallel$ and a_i represent the substrate and epilayer lattice constants, respectively. Also, the Poisson's ratio $D=2C_{12}/C_{11}$ where C_{11} and C_{12} are elastic constants [38]. Considering $\epsilon=e_{xx}-e_{zz}$ the directional cosines change to $(l,m,n)=(1+\epsilon,1+\epsilon,1-2\epsilon)/\sqrt{3}$. As a result, $V_{XX}=V_{YY}$, but these are not equal to

V_{ZZ}. Using Eq. (A5) it is then possible to show the effect of biaxial strain on the band structure.

Under biaxial tension as the bond rotates towards the x-y plane, the overlap between the p_x/p_y orbitals of the two atoms increases whereas overlap of the p_z orbitals decreases. The azimuthal angles θ_x and θ_y decrease whereas θ_z increases. One can think of the p_x/p_y orbitals of the two atoms becoming more head on whereas p_z orbitals becoming more parallel. This increases the contribution of the σ components of the p_x/p_y orbitals and weakens for the p_z orbital. On the contrary, the contribution of the π bond of the p_z orbital overlap increases but diminishes for the p_x/p_y orbitals. As a result, V_{XX} and V_{YY} will increase whereas V_{ZZ} will decrease as can be inferred by placing the values of the directional cosines in Eq. (A5). Using Eq. (A4) we can then see that the HH states go down whereas the LH states go up under biaxial tension. The situation is reversed under biaxial compression. The bond rotates away from the x-y plane increasing θ_x/θ_y and reducing θ_z. This, in turn, leads to lower V_{XX}/V_{YY} and higher V_{ZZ}. As a result, HH bands rise in energy whereas LH states go down. This simplified picture explains the movement of the bands in the InAlAs digital alloy, and, subsequently, the essential physics of the minigap formation in the sp^3 basis.

[1] A. Tosi, N. Calandri, M. Sanzaro, and F. Acerbi, IEEE J. Sel. Top. Quantum Electron. **20**, 192 (2014).

[2] J. C. Campbell, 8-advances in photodetectors, in *Optical Fiber Telecommunications VA*, Fifth ed., Optics and Photonics, edited by I. P. Kaminow, T. Li, and A. E. Willner (Academic, Burlington, MA, 2008), pp. 221–268.

[3] N. Bertone and W. Clark, Laser Focus World **43** (2007).

[4] P. Mitra, J. D. Beck, M. R. Skokan, J. E. Robinson, J. Antoszewski, K. J. Winchester, A. J. Keating, T. Nguyen, K. K. M. B. D. Silva, C. A. Musca, J. M. Dell, and L. Faraone, in *Intelligent Integrated Microsystems*, edited by R. A. Athale and J. C. Zolper, International Society for Optics and Photonics (SPIE, Bellingham, WA, 2006), pp. 70–80.

[5] G. M. Williams, Opt. Eng. **56**, 031224 (2017).

[6] M. Nada, F. Nakajima, T. Yoshimatsu, Y. Nakanishi, S. Tatsumi, Y. Yamada, K. Sano, and H. Matsuzaki, Appl. Phys. Lett. **116**, 140502 (2020).

[7] K. Pasquinelli, R. Lussana, S. Tisa, F. Villa, and F. Zappa, IEEE Sens. J. **20**, 7021 (2020).

[8] D. Thomson, A. Zilkie, J. E. Bowers, T. Komljenovic, G. T. Reed, L. Vivien, D. Marris-Morini, E. Cassan, L. Virot, J.-M. Fédéli, J.-M. Hartmann, J. H. Schmid, D.-X. Xu, F. Boeuf, P. O'Brien, G. Z. Mashanovich, and M. Nedeljkovic, J. Opt. **18**, 073003 (2016).

[9] J. C. Campbell, J. Lightwave Technol. **34**, 278 (2016).

[10] R. McIntyre, IEEE Trans. Electron Devices **ED-13**, 164 (1966).

[11] M. Teich, K. Matsuo, and B. Saleh, IEEE J. Quantum Electron. **22**, 1184 (1986).

[12] N. Z. Hakim, B. E. A. Saleh, and M. C. Teich, IEEE Trans. Electron Devices **37**, 599 (1990).

[13] J. Zheng, Y. Tan, Y. Yuan, A. Ghosh, and J. Campbell, J. Appl. Phys. **125**, 082514 (2019).

[14] S. R. Bank, J. C. Campbell, S. J. Maddox, A. K. Rockwell, M. E. Woodson, M. Ren, A. Jones, S. March, J. Zheng, and Y. Yuan, in *2018 IEEE Research and Applications of Photonics in Defense (RAPID)* (IEEE, Piscataway, NJ, 2018), pp. 1–3.

[15] X. Yi, S. Xie, B. Liang, L. W. Lim, J. S. Cheong, M. C. Debnath, D. L. Huffaker, C. H. Tan, and J. P. David, Nat. Photonics **13**, 683 (2019).

[16] J. Zheng, S. Z. Ahmed, Y. Yuan, A. Jones, Y. Tan, A. K. Rockwell, S. D. March, S. R. Bank, A. W. Ghosh, and J. C. Campbell, InfoMat **2**, 1236 (2020).

[17] J. Zheng, Y. Yuan, Y. Tan, Y. Peng, A. Rockwell, S. R. Bank, A. W. Ghosh, and J. C. Campbell, Appl. Phys. Lett. **115**, 171106 (2019).

[18] J. Zheng, Y. Yuan, Y. Tan, Y. Peng, A. K. Rockwell, S. R. Bank, A. W. Ghosh, and J. C. Campbell, J. Lightwave Technol. **36**, 3580 (2018).

[19] S. Z. Ahmed, Y. Tan, J. Zheng, J. C. Campbell, and A. W. Ghosh, Phys. Rev. Appl. **17**, 034044 (2022).

[20] D. J. Chadi and M. L. Cohen, Phys. Status Solidi (B) **68**, 405 (1975).

[21] W. A. Harrison, *Electronic Structure and the Properties of Solids: The Physics of the Chemical Bond* (Courier, New York, 2012).

[22] Y. Tan, M. Povolotskyi, T. Kubis, T. B. Boykin, and G. Klimeck, Phys. Rev. B **94**, 045311 (2016).

[23] Y. P. Tan, M. Povolotskyi, T. Kubis, T. B. Boykin, and G. Klimeck, Phys. Rev. B **92**, 085301 (2015).

[24] Y. Tan, F. W. Chen, and A. W. Ghosh, Appl. Phys. Lett. **109**, 101601 (2016).

[25] T. B. Boykin, N. Kharche, and G. Klimeck, Phys. Rev. B **76**, 035310 (2007).

[26] T. B. Boykin, N. Kharche, G. Klimeck, and M. Korkusinski, J. Phys.: Condens. Matter **19**, 036203 (2007).

[27] D. Kienle, J. I. Cera, and A. W. Ghosh, J. Appl. Phys. **100**, 043714 (2006).

[28] D. Kienle, K. H. Bevan, G. C. Liang, L. Siddiqui, J. I. Cera, and A. W. Ghosh, J. Appl. Phys. **100**, 043715 (2006).

[29] J. Heyd, G. E. Scuseria, and M. Ernzerhof, J. Chem. Phys. **118**, 8207 (2003).

[30] S. Z. Ahmed, Y. Tan, D. S. Truesdell, B. H. Calhoun, and A. W. Ghosh, J. Appl. Phys. **124**, 154503 (2018).

[31] A. Ghosh, in *Nanoelectronics-a Molecular View*, World Scientific Series in Nanoscience and Nanotechnology (World Scientific, Singapore, 2016).

[32] J. A. Støvneng and P. Lipavský, Phys. Rev. B **49**, 16494 (1994).

[33] B. Stickler, *Theory and modeling of spin-transport on the microscopic and the mesoscopic scale* (na, 2013)

[34] Y. Peter and M. Cardona, *Fundamentals of Semiconductors: Physics and Materials Properties* (Springer, Berlin, 2010).

[35] S.-H. Wei and A. Zunger, Phys. Rev. B **60**, 5404 (1999).

[36] F. H. Pollak and M. Cardona, Phys. Rev. **172**, 816 (1968).

[37] C. G. Van de Walle and R. M. Martin, Phys. Rev. B **34**, 5621 (1986).
[38] C. G. Van de Walle, Phys. Rev. B **39**, 1871 (1989).
[39] S.-H. Wei and A. Zunger, Phys. Rev. B **57**, 8983 (1998).
[40] P. R. C. Kent, G. L. W. Hart, and A. Zunger, Appl. Phys. Lett. **81**, 4377 (2002).
[41] G. Bir and G. Pikus, *Symmetry and Strain-Induced Effects in Semiconductors* (Wiley, New York, 1974).
[42] C. Mailhiot and D. Smith, J. Vac. Sci. Technol., A **7**, 445 (1989).
[43] Y. Sun, S. E. Thompson, and T. Nishida, J. Appl. Phys. **101**, 104503 (2007).
[44] J. C. Slater and G. F. Koster, Phys. Rev. **94**, 1498 (1954).